Acta Biomaterialia xxx (2013) xxx–xxx

Contents lists available at ScienceDirect

Acta Biomaterialia

journal homepage: www.elsevier.com/locate/actabiomat

Nanostructure of carious tooth enamel lesion

Hans Deyhle [a,b], Shane N. White [c], Oliver Bunk [b], Felix Beckmann [d], Bert Müller [a,*]

[a] Biomaterials Science Center, University of Basel, c/o University Hospital, 4031 Basel, Switzerland
[b] Swiss Light Source, Paul Scherrer Institut, 5232 Villigen, Switzerland
[c] UCLA School of Dentistry, University of California, Los Angeles, CA 90095-1668, USA
[d] Institute of Materials Research, Helmholtz-Zentrum Geesthacht, 21502 Geesthacht, Germany

ARTICLE INFO

Article history:
Received 22 April 2013
Received in revised form 6 July 2013
Accepted 13 August 2013
Available online xxxx

Keywords:
Enamel nanostructure
Smooth surface caries
Small-angle X-ray scattering
Human tooth
Synchrotron radiation

ABSTRACT

Carious lesions exhibit a complex structural organization composed of zones of higher and lower mineralization, formed by successive periods of cyclic de- and re-mineralization. A thorough understanding of the lesion morphology is necessary for the development of suitable treatments aiming to repair rather than replace the damaged tissue. This detailed understanding includes the entire lesion down to individual crystallites and nanopores within the natural organization of the crown. A moderate lesion, with surface loss and reaching dentin, and a very early lesion were studied. Scanning small-angle X-ray scattering (SAXS) with a pixel size of $20 \times 20\ \mu m^2$ was used to characterize these lesions, allowing for the identification of distinct zones with varied absorption and scattering behavior, indicative of varied porosity and pore morphology. Despite these differences, the overall orientation and anisotropy of the SAXS signal was unaltered throughout both lesions, indicating that an anisotropic scaffold is still present in the lesion. The finding that crystallite orientation is preserved throughout the lesions facilitates the identification of preventive re-mineralizing strategies with the potential to recreate the original nanostructure.
© 2013 Acta Materialia Inc. Published by Elsevier Ltd. All rights reserved.

1. Introduction

Caries is the most prevalent of all chronic childhood diseases and the leading cause of tooth loss among young adults in many societies [1–3]. Caries causes considerable suffering, loss of function and the need for costly restorative, endodontic and prosthetic interventions. However, behavioral, dietary, preventive and interventional actions can re-mineralize early lesions [4–6]. Improved knowledge of the carious process, de- and re-mineralization, at the component or nano-structural level could facilitate improved preventive and therapeutic approaches for early lesions and allow moderate lesions to be addressed.

Caries is a chronic hard tissue infection [7]. Smooth surface caries has been studied extensively, not just because of its epidemiological importance, but also because a relatively simple geometry facilitates studies and experimental modeling. Lesions have been studied in many ways, including macroscopic examination, hard tissue histology, light microscopy, scanning and transmitted electron microscopy, microradiography, micro and nano indentation, histochemical, microbiological and chemical analyses, and X-ray imaging techniques [8–19]. These methods have provided a wealth of information and allowed various zones to be identified. Electron microscopy has been used to observe microstructural changes such as clefts or channels in incipient lesions and to identify de- and re-mineralization-induced changes to individual crystallites, but generally only after they have been removed from their original spatial organizational positions and associations with their neighbors. Detailed understanding, or mapping, of the entire lesion at the level of individual crystallites and porosities remains elusive.

Differences in optical birefringence caused by the submicroscopic pores produced during de-mineralization have been used to divide the smooth surface lesion into four zones [15,20,21]: first, an outer surface layer of intact relatively unaffected enamel, displaying negative birefringence to polarized light, radio-opacity, with some focal holes and ~10% mineral loss; second, the body of the lesion, with positive birefringence to polarized light, radiolucency and substantial mineral loss of ~24%; third, the dark zone, with positive birefringence to polarized light, radio-opacity and ~6% of mineral loss; finally, the translucent zone with negative birefringence to polarized light, radio-opacity and only ~1% mineral loss. However, this classification does not describe changes in crystallite structure or organization. Furthermore, smaller and deeper pores are not discerned by birefringence [22].

Small-angle X-ray scattering (SAXS) is capable of delivering structural information about macromolecules or crystallites and of repeat distances in partially ordered systems as small as a few nanometers in size and up to several hundred nanometers [23–33]. This range is well suited to studying hydroxyapatite crystallite and collagen periodicities, the primary components of tooth structure. The combination of SAXS with real-space scanning [34] allows for the investigation of a tooth's nano-structural

* Corresponding author. Tel.: +41 (0) 61 265 9660; fax: +41 (0) 61 265 9699.
E-mail address: bert.mueller@unibas.ch (B. Müller).

1742-7061/$ - see front matter © 2013 Acta Materialia Inc. Published by Elsevier Ltd. All rights reserved.
http://dx.doi.org/10.1016/j.actbio.2013.08.024

components over extended areas through the acquisition of thousands scattering patterns [23,29–31,35,36]. Two-dimensional (2-D) maps with raster-scan step sizes as small as $0.1 \times 0.1\ mm^2$ have been made [31]. Because an early carious lesion may be only 0.1–0.2 mm in total thickness, and because features within a moderate lesion may be <0.1 mm thick, increased point density is needed to study the four zones generally used to describe smooth surface caries. Scanning SAXS with raster-scan step sizes of $20 \times 20\ \mu m^2$ is applied. This high point density allows the identification and comparison of morphological differences within and among carious zones with respect to structural organization: orientation and degree of anisotropy of the nanometer-size components.

2. Materials and methods

2.1. Carious specimens

Two representative naturally occurring smooth surface carious lesions, moderate and early, obtained from two third molars extracted for clinical reasons, were studied. All procedures were conducted in accordance with the Declaration of Helsinki and according to the ethical guidelines of the Canton of Basel, Switzerland. Teeth were extracted for clinical reasons unrelated to the study. Written consent by the patients concerning use of the extracted teeth is given in the patient entry form of the dental school. The consent is not study specific. Teeth are anonymized. Backtracking of patient identity is impossible and not desired. The moderate lesion (specimen H) had slight surface loss and appeared to barely reach beyond the dentino-enamel junction (DEJ). The early lesion (specimen V) was smaller and incipient, without surface breakdown, and limited to the outer third of the enamel. The tooth slices were cut using a diamond band saw (Exakt Apparatebau GmbH, Norderstedt, Germany). A 200 μm thin slice was cut in a transverse direction through the moderate lesion, while a 200 μm thin slice was obtained through the early lesion in the buccal-lingual direction (see Fig. 1). The slices were stored in phosphate buffered saline before and during measurements.

2.2. Conventional micro computed tomography

Micro computed tomography (μCT) data sets of the entire teeth were acquired with a Skyscan 1174™ tabletop scanner (Bruker, Belgium), and 900 projections with a pixel size of 35.6 μm were acquired over 360°. The acceleration voltage was set to 50 kV and the beam current to 800 μA. The data were reconstructed using a modified Feldkamp algorithm (NRecon, Bruker, Belgium).

2.3. Synchrotron radiation-based μCT

Synchrotron radiation-based μCT (SRμCT) measurements were performed at the W2 beamline at HASYLAB (DESY, Hamburg, Germany) operated by the HZG research center [37]. For specimen V, the photon energy was set to 45 keV, and 1440 equiangular projections with a pixel size of 4.6 μm were acquired over 360°. The rotation axis was chosen asymmetrical to the incoming X-ray beam to allow for a larger field of view [38]. The data were reconstructed using a filtered backprojection algorithm. Specimen H was measured at a photon energy of 30 keV. The pixel size of the projections corresponded to 3.2 μm, and 900 projections were acquired over 180°.

2.4. SAXS data acquisition

Scanning SAXS measurements were performed at the cSAXS beamline [39] of the Swiss Light Source (Paul Scherrer Institute, Villigen, Switzerland). The specimens were stored in polyimide sachets and placed on an aluminum holder. Scattering patterns were acquired in a raster scan fashion in the *x*- and *y*-directions perpendicular to the beam. For specimen V, the points at which SAXS data was acquired were 50 μm apart in both *x*- and *y*-directions, while for specimen H, a raster scan step size of 20 μm was chosen. The photon energy was set to 18.6 keV. The scanning in the horizontal, i.e., *x*-, direction was performed with the detector recording a series of SAXS data, while the specimens moved at a velocity of 1.786 and 0.714 mm s^{-1}, respectively. The X-ray beam was focused to 25 μm × 8 μm full width at half-maximum (FWHM) spot size at the specimen position. In the first scan, the X-ray transmission of the specimens at each scanning position was recorded with no beam stop and an attenuated beam with 8 ms exposure time. In the second scan, the scattering patterns were recorded with two modules of the PILATUS 2 M detector [40] with 20 ms exposure time and 8 ms readout time. For specimen V, 32,000 frames were acquired, and for specimen H, 82,000 frames. The direct beam was covered with a beam stop 3 mm in diameter. The transmission data were used to correct the SAXS signal for specimen absorption. The specimen–detector distance of 7140 mm was determined with the first-order diffraction ring of a silver-behenate powder. To minimize air scattering, an evacuated flight tube was placed between specimen and detector.

2.5. SAXS data treatment

Each scattering pattern is divided into 16 azimuthal sectors, and the intensity is azimuthally integrated at each radial position, yielding, for each scattering pattern, intensities for the 16 segments as a function of q. The intensity in each segment for a chosen radial range, plotted against the segment angular position ϕ, is approximated with a cosine by means of fast Fourier transform:

$$I(\phi) = I_0 + I_2 \cos(\phi + \Phi) \tag{1}$$

where I_0 and I_2 are the norm of the zero and second Fourier components, respectively, and Φ is the phase of the second Fourier component. The data treatment is explained in detail elsewhere [39]. The data were treated using self-written MATLAB® (2011, The MathWorks, Natick, USA) routines.

The SAXS signal along radial lines through the carious lesions was plotted from 0° to 45° in the direction of maximum extension of the lesion in 15° increments. Control plots of sound tooth structure were made along radial lines of the same specimen, but because natural caries was studied, the control plots could not be made at the same site as the caries. Therefore, the control samples inevitably differed slightly from the carious samples with respect to enamel and dentin thickness and radius of curvature. Additionally, because the moderate caries specimen had lost some surface enamel, its outer endpoint, did not coincide with that of the intact controls. The following data fields were examined and plotted for sound control samples and for samples through the moderate and incipient carious lesions. The mean orientation of the scattering signal can be extracted from the phase term Φ given in Eq. (3). The orientation of the scattering signal is generally perpendicular to the main orientation of the scattering structures, e.g., crystallites in dentin and enamel.

3. Results

The SAXS study includes results from two representative examples of the carious process: a moderate lesion with surface loss reaching dentin with a horizontal orientation (specimen H); and an early surface lesion with a vertical orientation (V). Both examples are smooth surface lesions. Control samples were taken from healthy unaffected enamel in the same tooth specimens.

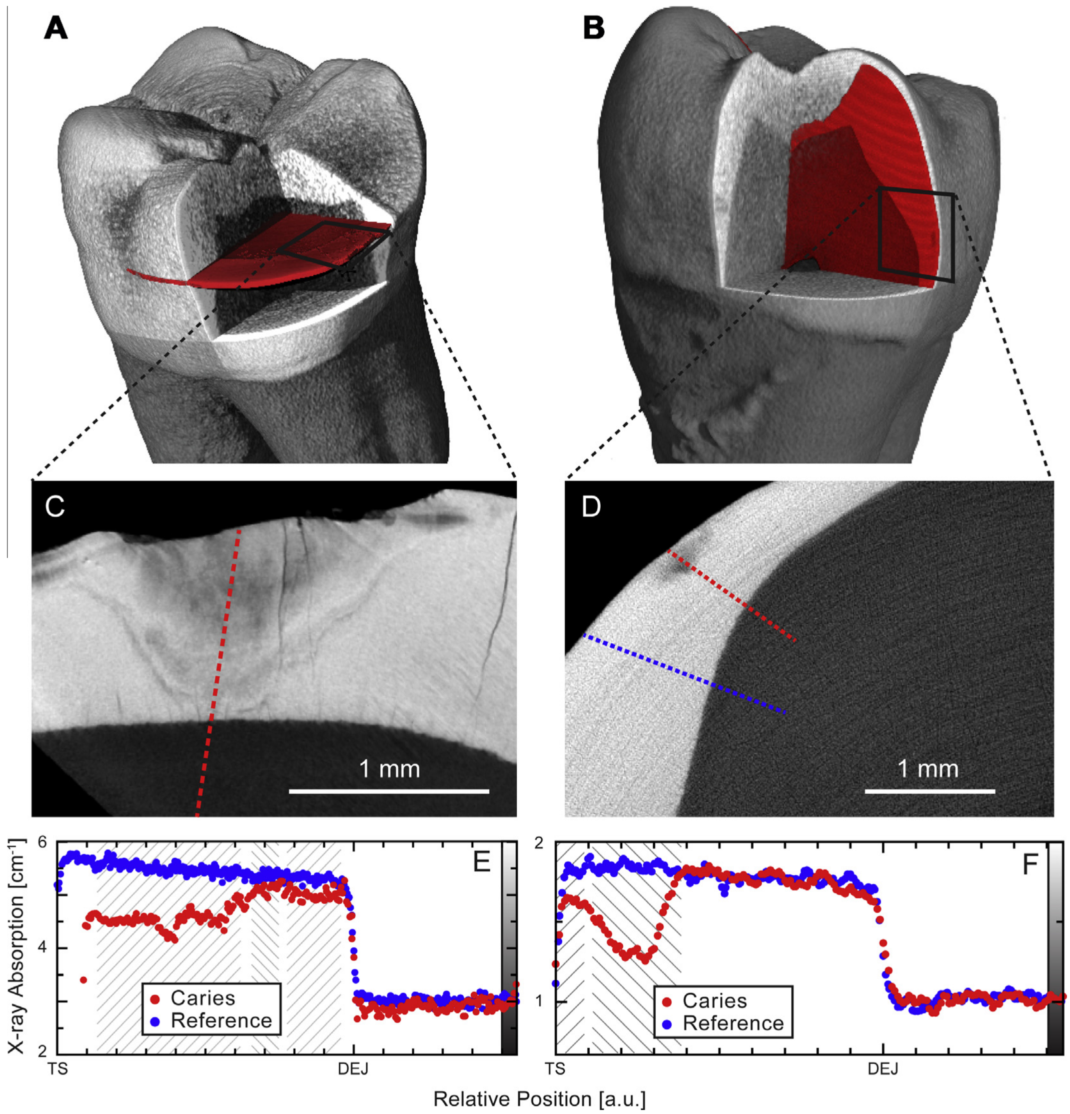

Fig. 1. (A, B) Position of specimens H and V in a 3-D μCT rendering of the teeth. (C, D) Selected virtual cuts through the SRμCT data of the tooth slices. The carious lesion in specimen H (C) can be identified as darker region in the enamel, extending from the TS to the dentin. The funnel-shaped subsurface lesion in specimen V (D) appears as darker spot near the outer limit of the enamel. (E, F) Line plots of X-ray absorption through the specimens according to the dashed lines in (B) and (C), respectively. The line through unaffected enamel in specimen H (C) lies outside the field of view. The abscissa was rescaled so that both the DEJ and TS were superimposed.

3.1. Moderate lesion reaching dentin, specimen H

Fig. 1 shows the position of specimens H and V within the corresponding teeth, in a three-dimensional (3-D) μCT rendering. Specimen H presented a moderate lesion extending to the dentin, as visible in the SRμCT slice (Fig. 1C). The outermost surface enamel (zone 1) was intact at the peripheral borders of the lesion, but was absent from the central part of the lesion, probably as a result of the carious process. Within the remaining carious lesion, three additional zones were discerned; these were described by a profile of X-ray absorption through the center of the lesion (Fig. 1E). Zone 2 extended through half the thickness of the enamel and exhibited the lowest X-ray density, with a mean absorption corresponding to 86% of that of comparable unaffected enamel, and minima of 76%. Zone 3, a narrower band, deeper than and surrounding the first zone, showed X-ray absorption comparable with that of unaffected enamel, especially towards the sides of the lesion. Finally, zone 4, adjacent to the second and reaching the dentin, again displayed slightly decreased absorption with respect to unaffected enamel, with a mean of 93% and minima of 88%. Bands of alternating X-ray absorption could be seen in the deeper parts of the lesions on both sides of its deepest extension.

The total scattered intensity is described in Fig. 2. Fig. 2A–C shows the intensity of the scattering signal on a line through the lesion (red dots) and one through unaffected enamel (blue dots), in the q ranges corresponding to 10–20 nm, 100–110 nm and 190–200 nm, respectively. The momentum transfer q is defined as $q = \frac{4\pi}{\lambda}\sin(\theta)$, where λ is the wavelength of the scattering X-rays, and θ is the half scattering angle. q is related to the real space periodicity d by $q = \frac{2\pi}{d}$. Fig. 2D shows three profiles through unaffected enamel at different positions in the specimen (cf., image bottom right) in the range 100–110 nm. The abscissae of the plots were rescaled so that both the DEJ and tooth surface (TS) were superimposed. Little difference in scattered intensity plots could be discerned among the unaffected control samples.

Within the moderate carious lesion, distinct scattering intensity zones were discerned; they were largely coincident with the absorption zones, and are indicated by the shaded regions in Fig. 2A–C. Zone 2 exhibited high scattering in the body of the lesion, extending through half the enamel thickness; zone 3 was

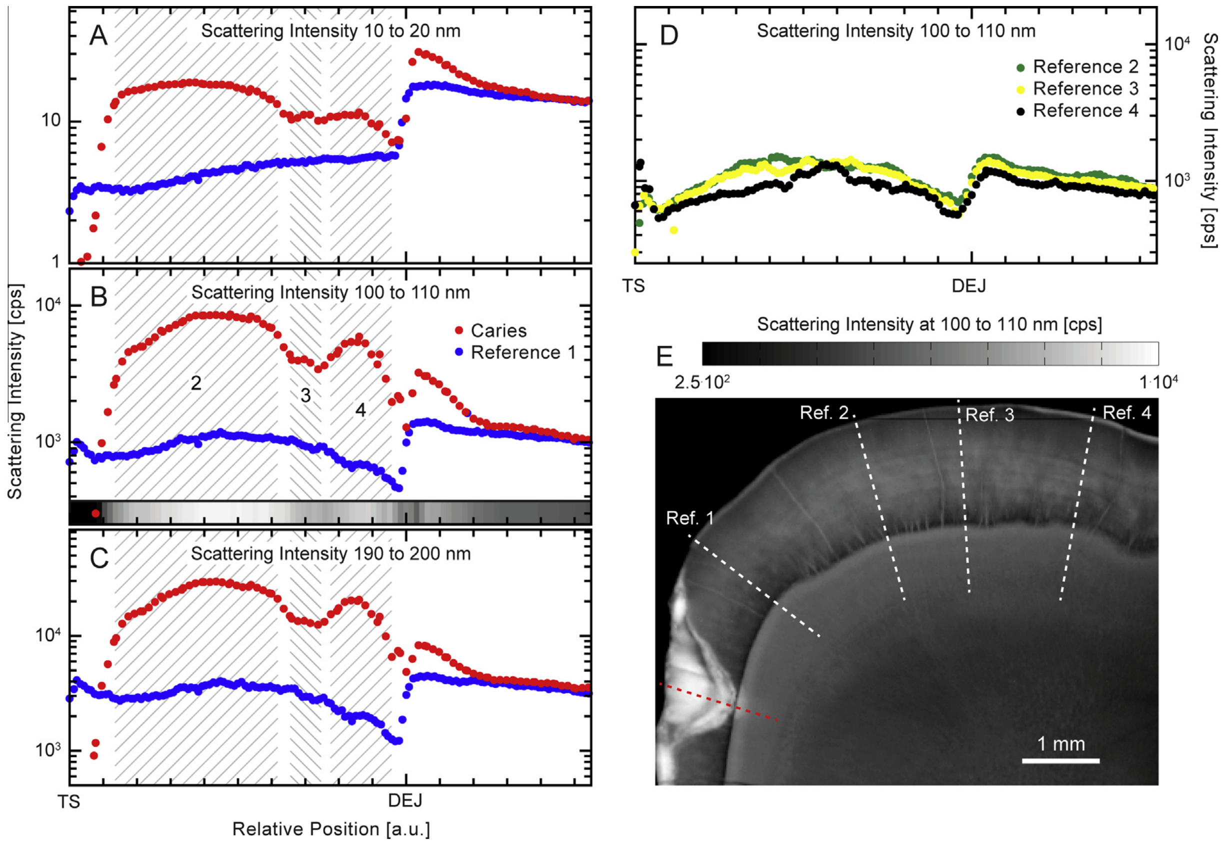

Fig. 2. (A–C) Intensity of the scattering signal on a line through the lesion (red dots) and one through unaffected enamel (blue dots), in the ranges 10–20 nm, 100–110 nm and 190–200 nm, of specimen H, in counts per second according to the dashed lines in (E). Distinct scattering intensity zones can be discerned within the lesion, indicated by the shaded regions. (D) Three line plots through unaffected enamel at different positions in the specimen in the range 100–110 nm to demonstrate their similarity. (E) 2-D map of the total scattering intensity at scattering angles corresponding to the range 100–110 nm.

an intermediate band with reduced scattering; and zone 4 a region with increased scattering, approached the DEJ. Scattering intensities from zones 3 and 4 became more and more alike for smaller features in the 10–20 nm range. No such zones were found in unaffected healthy enamel over the ranges examined (Fig. 2A–D). The total scattered intensity of sound unaffected bulk enamel was almost an order of magnitude lower than the peak signal at the center of the body of the carious lesion. Table 1 summarizes the optical and X-ray scattering behavior of each zone.

As for all the plots in the present paper, additional data sets were created along lines rotated ±15° from the central lines through the maximum extensions of the lesions depicted in Figs. 2 and 4–6 (data not shown). Little difference was found between these additional lines and the central lines; angled lines simply produced more oblique images of the same features.

In the narrow region of the DEJ interface, the plots of carious and unaffected control samples intersected (Fig. 2A–C). However, increased scattering intensity was found in the affected region of dentin immediately beneath the DEJ (Fig. 2A–C).

Scattered intensities for points belonging to the three carious zones (I_{car}) and points from anatomically similar regions in healthy enamel (I_{sound}) are compared in Fig. 3A. The ratio I_{car}/I_{sound} is plotted as a function of momentum transfer q. Zones 1 and 2 presented similar behavior, the ratio I_{car}/I_{sound} being constant over all but the smallest examined q ranges corresponding to periodicities <50 nm. For zone 2, I_{car}/I_{sound} amounted to about two-thirds of I_{car}/I_{sound} of zone 1. Zones 2 and 4 behaved in a like manner at periodicity ranges >100 nm. For smaller periodicities, the intensity in zone 4 decreased more rapidly than in zones 2 and 3.

The mean orientation of scattering patterns [39] is displayed in Fig. 4. The color in the image (Fig. 4E) shows the orientation of the main scattering signal for each point according to the color wheel. The line plots show the orientation of the scattering signal with respect to the dashed lines indicated in Fig. 4E, with 0° indicating a

Table 1
Classification of carious zones comparing optical and X-ray scattering behavior.

	Pore size/ distribution	Birefringence ([15,20,21])	X-ray absorption (with respect to unaffected enamel)	Scattering potential (with respect to unaffected enamel)
Zone 1	intact enamel[a]	Negative	Approximating unaffected enamel[a]	Approximating unaffected enamel[a]
Zone 2	Homogeneous pore size distribution between 50 and 200 nm	Positive	Reduced (∼75% of unaffected enamel)	Over one order of magnitude higher
Zone 3	Homogeneous pore size distribution between 50 and 200 nm	Positive	Approximating unaffected enamel	About five times higher
Zone 4	Prevalence of larger pores (here above 100 nm)	Negative	Slightly reduced (∼93% of unaffected enamel), with bands approximating unaffected enamel	Over one order of magnitude higher

[a] The statements concern specimen V.

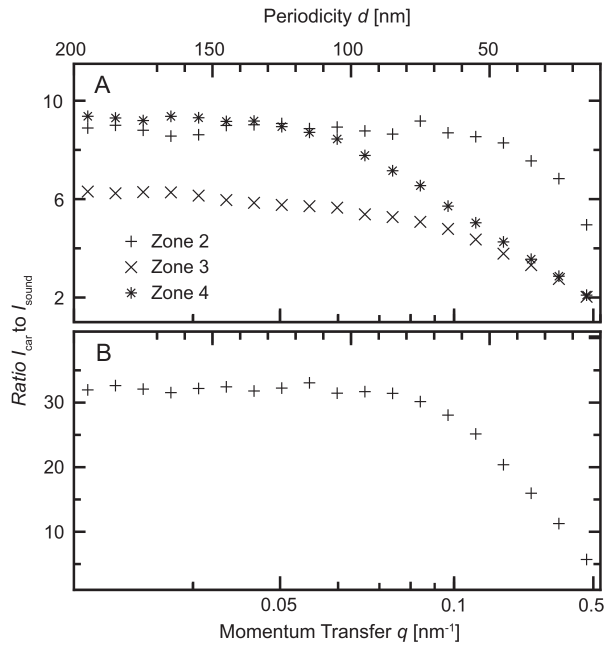

Fig. 3. (A) Ratio I_{car} to I_{sound} of the scattering signal of a representative point in each carious zone I_{car} to a comparable point in healthy unaffected enamel I_{sound} as a function of the feature size d for specimen H. (B) Ratio I_{car} to I_{sound} for one point inside the lesion and a corresponding point in healthy unaffected enamel of specimen V as a function of momentum transfer q.

parallel alignment. Fig. 4A–C shows the orientation of the scattering signal in the ranges 10–20 nm, 100–110 nm and 190–200 nm, respectively, along a line through the lesion. A plot through unaffected healthy enamel, showing the orientation of the scattering signal related to features between 100 and 110 nm, is shown in Fig. 4D. The abscissae of the plots were rescaled so that both the DEJ and TS were superimposed. Carious enamel samples and their sound unaffected controls exhibited remarkably little difference in their values over the range of periodicities studied.

Fig. 5D shows the azimuthal plot around the direct beam of the total scattered intensity in a radial range corresponding to 100–110 nm, for a point in the caries (red dots) and in unaffected enamel (blue dots). The SAXS intensity is localized mainly along the equatorial direction of the crystallites (i.e., parallel to the TS) in both carious and unaffected enamel, giving rise to two distinct peaks. The increased intensity of the scattering signal from carious enamel is almost solely associated with the direction perpendicular to the crystallites, whereas the increase in intensity observed in all other directions was an order of magnitude smaller. The width of the peaks is related to the anisotropy of the scattering features within the specimen. For each raster scan point, the peaks were fitted with Gaussians and a constant background, and the FWHM was extracted. Fig. 5E shows the FWHM for each point in the range corresponding to 100–110 nm. In zone 2, slight changes to the FWHM of the equatorial scattering can be identified. The red and blue dots indicate the points from which the azimuthal intensity distribution in Fig. 5A was plotted. Fig. 5A–C shows the FWHM of the equatorial peaks in the ranges 10–20 nm, 100–110 nm and 190–200 nm, respectively, along a line through the lesion (red dots) and a line through unaffected enamel (blue dots). A slight decrease in the FWHM, i.e., an increase in SAXS anisotropy, can be found in the carious region, especially towards larger nanometer periodicities.

3.2. Early surface enamel lesion, specimen V

The orientation of the section of interest within the tooth is displayed in Fig. 1B. Selected slices through the SRμCT data set of specimen V are shown in Fig. 1D. The carious lesion was visible as a small darker region in the sub-surface enamel owing to reduced X-ray absorption. No surface loss was evident. Line plots showed that the absorption of the outermost surface of the lesion, zone 1, approximated that of unaffected controls; the body of the lesion, zone 2, exhibited a definite subsurface dip in X-ray absorption (Fig. 1F). In all other ways, X-ray absorption did not differ among control and lesion plots.

Total scattered intensity is described in Fig. 6A for the range 100–110 nm, along a line through the lesion (red dots) and through unaffected enamel (blue dots). Plots for the other examined ranges exhibited equivalent behavior (data not shown). The small early carious lesion differed from the moderate carious lesion. The very outermost surface enamel, zone 1, indicated by the shaded region labeled 1, approximated the control samples, and a single narrow sharp spike in scattered intensity, the body of the lesion, was localized to the outer half of the enamel thickness, indicated by the shaded region labeled 2.

Fig. 3B, shows the ratio I_{car}/I_{sound} for a point inside the small lesion and a comparable point in healthy enamel, analogously to the three regions of the moderate lesion. The ratio keeps a constant value for periodicities down to 100 nm, and decreases towards larger scattering angles, analogous behavior to zone 2 in the moderate lesion.

The angle of scattering signals in the range 100–110 nm with respect to a radial line is displayed in Fig. 6C (through the carious lesion) and D (through healthy unaffected tissue). Little difference could be discerned between values from the carious region and their controls. These data are shown in separate plots for the sake of clarity. Plots for the other examined ranges exhibited equivalent behavior (data not shown). Anisotropy, as extracted from the FWHM of the equatorial scattering (cf., Fig. 5), is shown in Fig. 6B, along a line through the lesion (red dots), and one through unaffected enamel (blue dots). The FWHM for each raster scan point in the range 100–110 nm is shown in Fig. 6F. The carious lesion is visible as slightly darker zone near the TS.

4. Discussion

4.1. Zone classification

Absorption data were consistent with prior radiographic analyses. The small early lesion had a narrow dip in absorption that was sharply localized to a zone just beneath the relatively normal outermost enamel. These results suggest that, in these real-life carious lesions, the outermost enamel can readily re-mineralize, or even hyper-mineralize in an appropriate environment [7]. Many prior studies profiling carious lesions have shown increased X-ray density, increased mineralization, micro- and nano-hardness of zone 1 surface enamel [9,10,12–14,16,41–43]. Physicochemical phenomena and protection by saliva seem the most likely reasons for the fortification of the outermost enamel [7,44]. Although surface protection does not occur in all cases, it has been reported in both naturally occurring and artificial lesions [9,10,12–14,16,41–44]. However, re- or hyper-mineralization of the outermost enamel is a double-edged sword: it prevents substrates, calcium and phosphate ions, reaching the deeper parts of the lesion, thus preventing re-mineralization of deeper parts of the lesion. The moderate lesion demonstrated the additional complexity of the bulk and deepest parts of the enamel lesion being separated by an intermediate denser and thus less porous zone and containing several alternating layers or laminations, displayed as layers of alternating X-ray density (Fig. 1) [45]. The laminations may have been produced by successive periods of cyclic de- and re-mineralization over differing time periods when the environment may have favored one or other process [45].

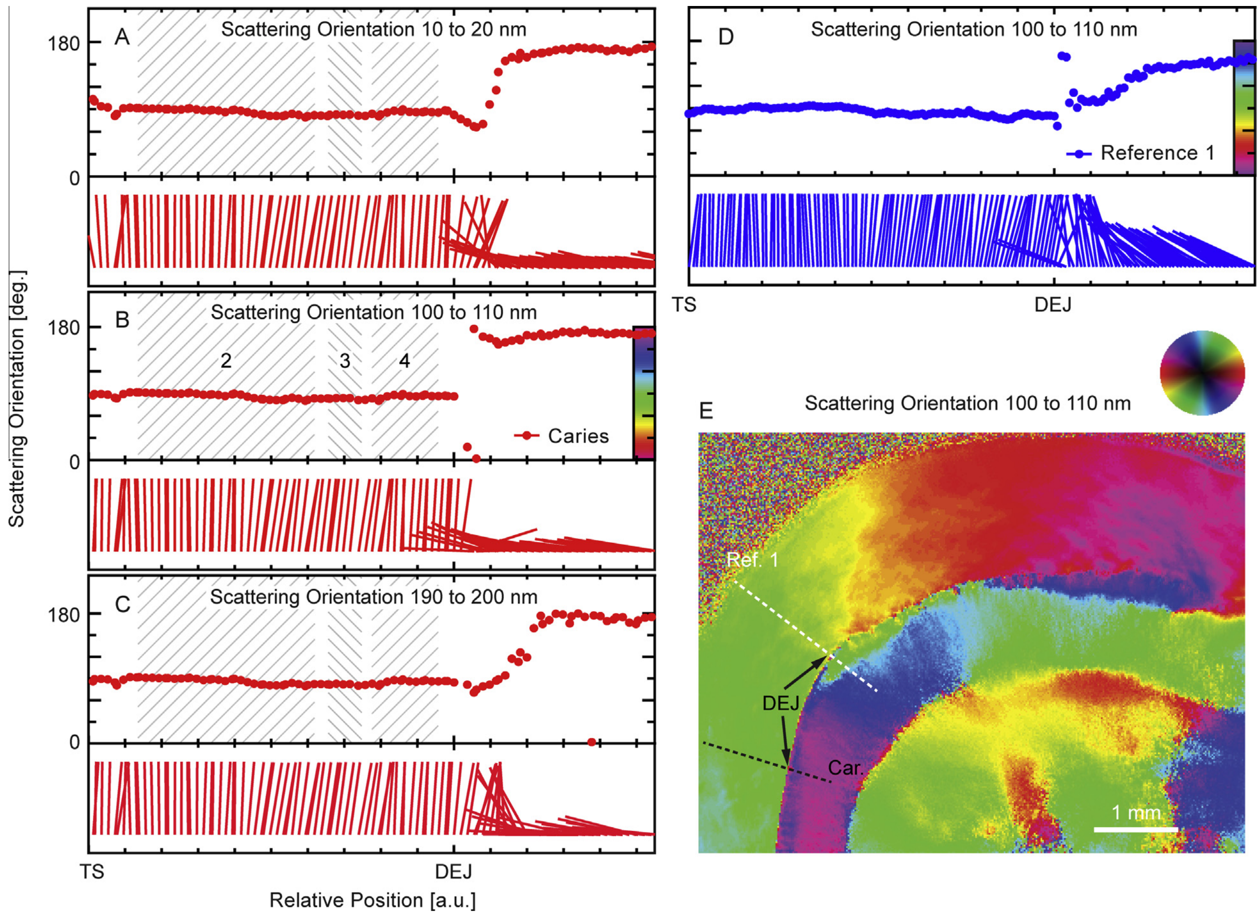

Fig. 4. (A–C) Orientation of the scattering signal along the black dashed line indicated in the image (E). The values given correspond to the angle between the main orientation of the scattering signal and the black dashed radial line, with 0° indicating a parallel alignment. Plots (A–C) show the orientation of the scattering signal in the ranges 10–20 nm, 100–110 nm and 190–200 nm, respectively. The vector plots demonstrate the perpendicular alignment of the scattering signal to the radial line in enamel. The shaded regions correspond to the zones as identified in Fig. 2. (D) Orientation of the scattering signal along a line through unaffected healthy enamel, in the range 100–110 nm, cf., white dashed line in (E). (E) 2-D map of the orientation of the scattering signal at scattering angles corresponding to the range 100–110 nm, according to the color wheel.

Differences in birefringence due to the production of submicroscopic pores during de-mineralization have been used to segment the smooth surface carious enamel lesion into four zones: the outer surface (zone 1), the body of the lesion (zone 2), the dark zone (zone 3), and the translucent zone (zone 4) [15,20,21]. Most of the outermost enamel surface of the moderate lesion, zone 1, had been lost and thus was not studied. However, the remaining lesion was divisible by absorption and scattering intensity into zones broadly coincident with those defined by differences in optical birefringence [15,20,21]. In the small early lesion, zones 1 and 2 were evident and broadly coincident with those defined by differences in optical birefringence.

Since both methods are sensitive to the presence of pores within the calcium phosphate phases of the enamel, the assumption that the zones coincide is reasonable. As optical birefringence, related to the wavelength of visible light, it is relatively sensitive to long-range orders in comparison with SAXS, the methods are complementary.

4.2. Pore size distribution

The increase in the abundance of pores in carious tooth structures must be considered to be a primary defining feature of the carious process. Accordingly, an increased scattered intensity in carious dentin [31] and enamel [35] has been reported. Since the SAXS signal intensity is not homogeneous across the thickness of the enamel, the ratio I_{car}/I_{sound} of the SAXS signal from the carious lesion and from an anatomically equivalent region was chosen to illustrate changes in scattering behavior.

In zone 4 of the moderate lesion, generally consistent with the translucent zone, I_{car}/I_{sound} decreased markedly <100 nm, indicative of larger pores. The fact that the I_{car}/I_{sound} was constant for all investigated nanometer ranges except the smallest ones <50 nm in both zones 2 and 3 suggests the presence of a more homogeneous distribution of pore sizes in the investigated range 200–50 nm.

It has been hypothesized that, in the outer regions of surface caries and, notably, in the dark zone (zone 3), some degree of re-mineralization occurs [46], or that the redistribution of endogenous organic material inside the lesion leads to increased mineral content [47]. This similar behavior of the ratio I_{car}/I_{sound} as a function of scattering angle in zones 2 and 3 is indicative of a similar caries-induced destruction pattern, consisting of larger and smaller pores, where the smaller ones are the result of partially re-mineralized larger voids [45,48]. The higher scattered intensity in zone 1 arises from a more advanced status of enamel deterioration, i.e., a higher density of pores, in agreement with its reduced X-ray density. The decreased number of pores in zone 2 is partly due to natural re-mineralization.

The findings represented in Figs. 1–6 are consistent with the traditional models of the carious lesion derived from light microscopy,

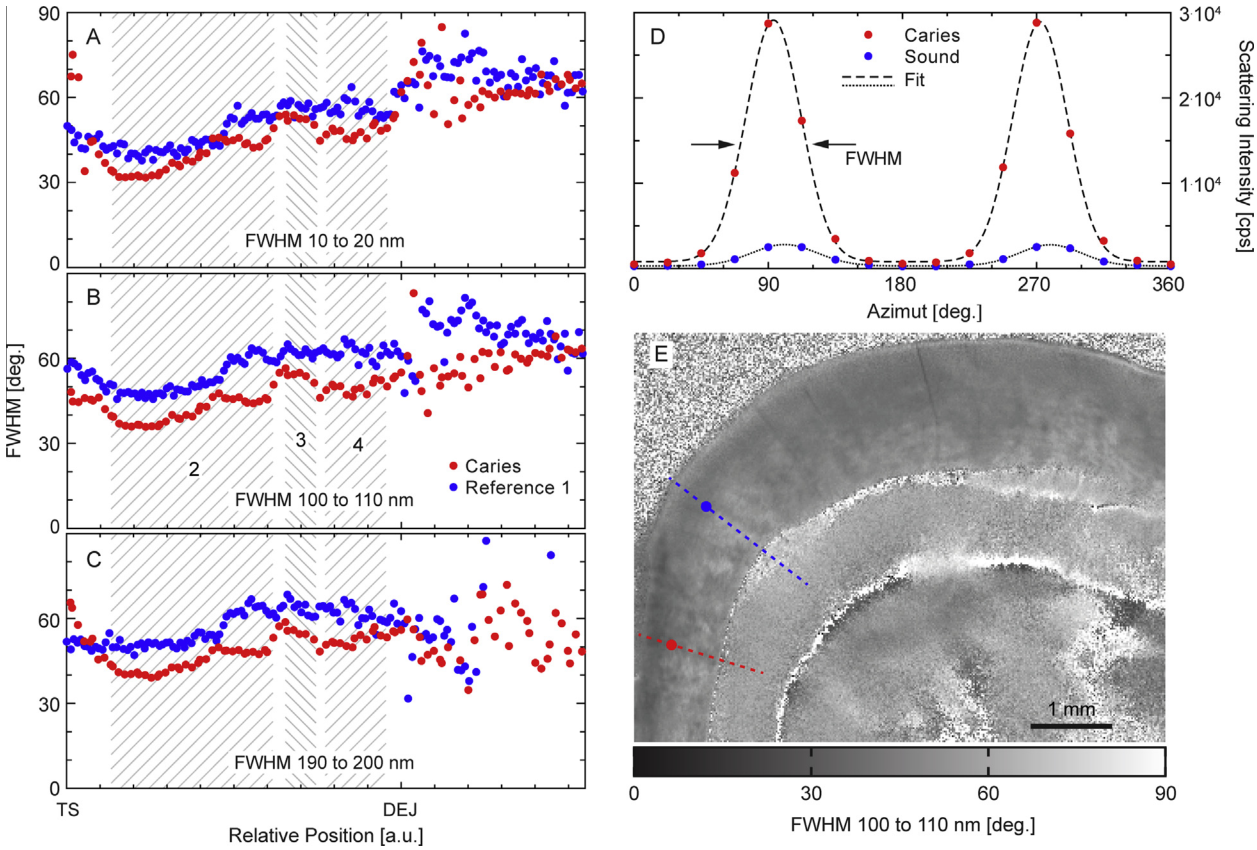

Fig. 5. (A–C) FWHM value of the azimuthal SAXS intensity distribution in the ranges 10–20 nm, 100–110 nm and 190–200 nm, respectively, along a line through the lesion (red dots) and one through unaffected enamel (blue dots, cf., (E)). The FWHM value determination is illustrated in (D). (D) SAXS intensity as function of the azimuthal angle around the central beam, for a point in the lesion (red-colored dots) and one in healthy enamel (blue-colored dots) of specimen H, according to (E). The intensity distribution was fitted with two Gaussians and a background. (E) The FWHM of the Gaussians was extracted for each raster scan point. Zone 1 of the lesion appears slightly darker than unaffected enamel, indicating increased anisotropy of the scattering signal.

microradiography and microhardness profiles [12], but have advanced knowledge in defining the underlying nanostructures.

Despite increased porosity and decreased density in the enamel and dentin immediately adjacent to the DEJ, the scattering intensity and absorption plots for carious and unaffected control samples intersected at this internal interface. The DEJ, a most remarkable structure, durably unites extremely dissimilar biomaterials, enamel and dentin, preventing crack propagation from brittle enamel into dentin, and preventing interfacial delamination [49–52]. This finding has extremely important implications for the restorative strategies used to address carious teeth, suggesting that ultraconservative approaches, beyond current minimally invasive approaches [53], could preserve an intact DEJ, even if bounded on both sides by partly de-mineralized tissues.

In the small early lesion, only a slight decrease in X-ray density in the outermost enamel was observed; whereas, the body of the lesion had a marked decrease. The scattering signal intensity presented a similar but inverse behavior, being comparable with that from healthy enamel at the surface of the tooth and increasing with decreasing X-ray density of the specimen. The I_{car}/I_{sound} behavior is similar to that found in the fourth, deepest zone in the moderate lesion. The ratio I_{car}/I_{sound} is higher for small scattering angles, i.e., periodicities >100 nm. This similarity indicates that both the subsurface body lesion and the deepest zone in the moderate lesion are cases of early caries attack, and a similar pore size distribution can be expected.

4.3. Nanostructure orientation and anisotropy

The mean orientation of the scattering signal remained unchanged among carious and sound tooth structure in both early and moderate carious lesions. The mean orientation of the scattering signal in healthy enamel was clearly related to the arrangement of the crystallites in the rods running from the DEJ towards TS, with their *c*-axis parallel to the crystallite long axis [54], the scattering signal being aligned perpendicularly to this direction. Apparently, the contribution of the interrod crystallites (rod sheaths and tails) is less than the scattering from the highly ordered and closely packed crystallites within the rod body [55–60].

As illustrated in Fig. 5, caries-induced changes only slightly modify the SAXS signal anisotropy, towards higher anisotropy. The distinction was more marked in zone 2, where the highest degree of de-mineralization was found. Similarly, in the subsurface lesion in specimen V, where the de-mineralization reached 25%, a slight increase in anisotropy was observed. Here, the selective hollowing [61] and complete dissolution of individual crystallites within the rods leads to the increased equatorial scattering, parallel to the DEJ, while increase in scattering signal from the more resistant interrod crystallites is less prominent. In zone 3, where a certain degree of re-mineralization has taken place, the FWHM of the SAXS approximates that of unaffected enamel, i.e., anisotropy is decreased compared with zone 2, indicating that re-deposition processes give rise to at least partially isotropic structures. While the convergence between the FWHM values in carious and healthy tissues might indicate the restoration of tooth morphology through the naturally occurring re-mineralization, this does not necessarily mean that this is actually the case, since it is impossible to determine from the SAXS signal whether the re-deposition of material is happening preferentially at certain locations, such as within the rod or the interrod. The SAXS signal appears highly anisotropic, however, indicating that despite de- and re-minerali-

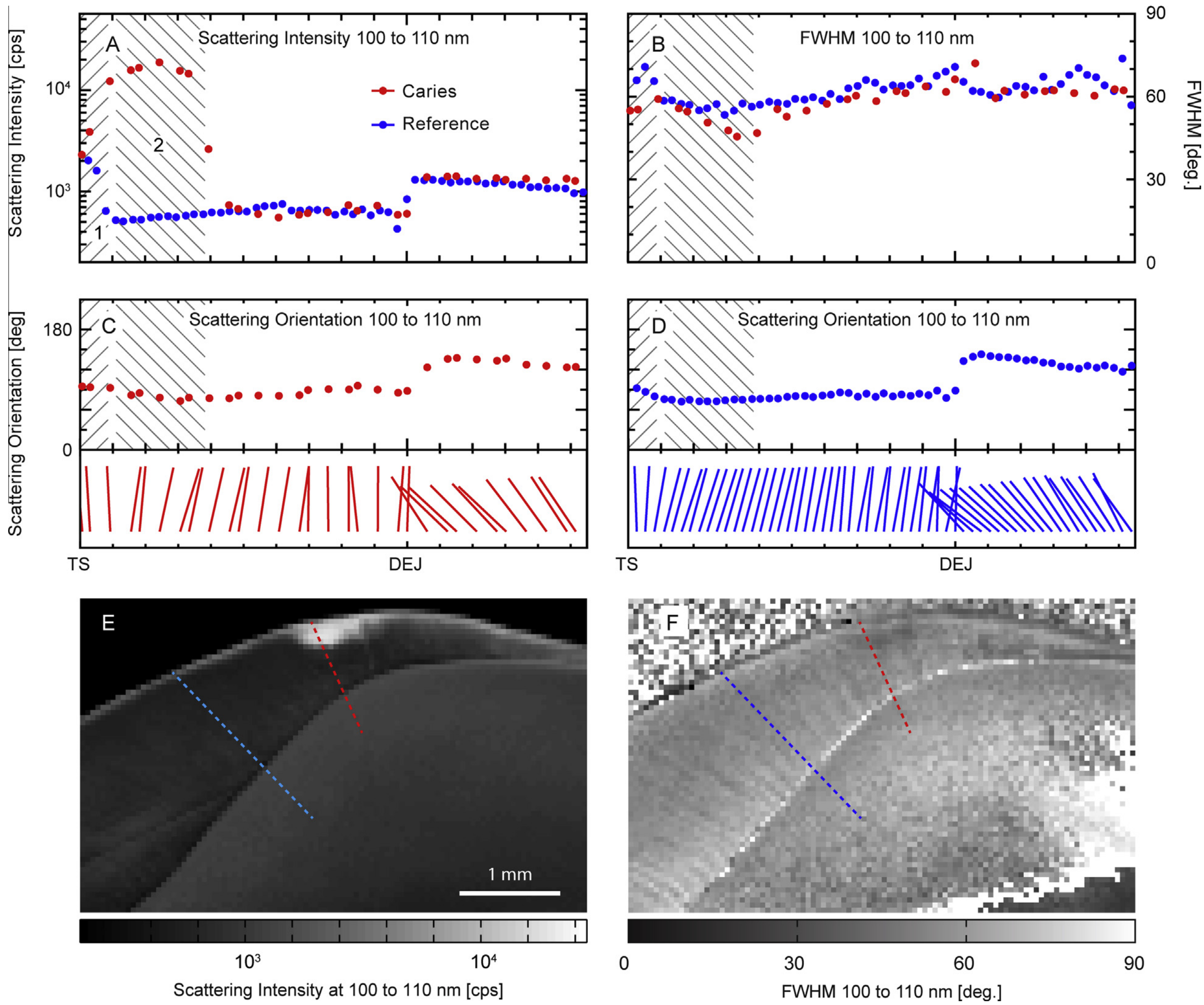

Fig. 6. Combined plots for specimen V. (A) Intensity of the scattering signal on a line through the lesion (red dots) and one through unaffected enamel (blue dots), in the range 100–110 nm, according to (E). The scattering signal in the outermost carious enamel, indicated by the shaded region labeled 1, approximates that of healthy enamel. The body of the carious lesion, located in the outer half of the enamel and indicated by the shaded region labeled 2, yields an increased scattering signal. (B) FWHM of the azimuthal intensity distribution of the scattering signal on a line through the lesion (red dots) and one through healthy enamel (blue dots), in the range 100–110 nm according to (F). The inner 50% of the lesion exhibits increased anisotropy, i.e., a reduced FWHM value. (C, D) Orientation of the scattering signal along a line through the lesion (C) and one through healthy enamel (D), in the range 100–110 nm according to (E), with respect to the dotted lines in (E). The carious lesion cannot be readily distinguished. (E) 2-D map of the total scattered intensity in the range 100–110 nm for specimen V. The carious lesion appears as a bright spot at the enamel surface. (F) 2-D map of the FWHM of the azimuthal intensity distribution in the range 100–110 nm. The lesion exhibits slightly increased anisotropy compared with unaffected enamel.

zation processes in zone 3 much of the enamel nanostructure is retained. Zone 4 presents FWHM values close to those from unaffected enamel. Since only little re-mineralization can be expected in zone 4, it appears that, despite caries-induced destruction, the structural anisotropy of the affected enamel is preserved. The retention of organization, despite de-mineralization, has important implications for the potential for interventions to not only re-mineralize de-mineralized enamel, but to do so in the original organizational form at the nanostructural level.

4.4. Confluence with classical caries models

Although the sample size was small, the lesions studied were carefully chosen to bracket the classically studied early carious lesion. The examination was performed in different perpendicular planes. The caries lesions were natural, probably occurring over years with innumerable cycles of de-mineralization and re-mineralization, rather than being artificially produced. They complemented prior SAXS data on fissure caries and an advanced grossly cavitated lesion. Instead of a small amount of data on a large sample, this work produced an enormous amount of data (over 110,000 frames) on a small, but well-anchored, sample. It is important to note that the findings with respect to unaltered enamel were completely consistent with prior SAXS data on a variety of other teeth [33]; the data describing the studied lesions, early and moderate, in different planes, were entirely consistent with one-another and with classical models [9,10,12,14–16,20,21,31,35,41–43,45]. The findings were consistent with SAXS data previously reported for an advanced cavitated lesion and for fissure caries [33,36].

5. Conclusions

The fact that both orientation and anisotropy of the SAXS signal from carious enamel closely resembled those from unaffected regions reinforces the notion that naturally occurring de- and re-mineralization produce an anisotropic structure that retains the original nanoscale organization. This current SAXS data, demonstrating the preservation of orientation in carious lesions, independent of degree of de-mineralization or pore morphology over 20–200 nm, advances understanding of the effects of de- and re-mineralization cycles at the crystallite level.

Acknowledgments

The support of F. Schmidli (Basel) during specimen preparation and acquisition of the light microscopy images is gratefully acknowledged. Beamtime at HASYLAB was granted under proposal number I-20080224 EC. The SAXS experiments were performed on the cSAXS beamline at the Swiss Light Source, Paul Scherrer, Institut, Villigen, Switzerland. Extracted teeth were kindly provided by dentists G. Krastl and N. Zitzmann (Basel).

Appendix A. Figures with essential color discrimination

Certain figures in this article, particularly Fig. 2, are difficult to interpret in black and white. The full color images can be found in the on-line version, at http://dx.doi.org/10.1016/j.actbio.2013.08.024

References

[1] Bagramian RA, Garcia Godoy F, Volpe AR. The global increase in dental caries. A pending public health crisis. Am J Dent 2009;22:3–8.
[2] Dye BA, Li X, Thornton-Evans G. Oral health disparities as determined by selected healthy people 2020 Oral Health Objectives for the United States, 2009–2010. NCHS Data Brief 2012;104:1–7.
[3] Petersen PE. Challenges to improvement of oral health in the 21st century - the approach of the WHO Global Oral Health Programme. Int Dent J 2004;534:329–43.
[4] Head JA. A study of saliva and its action on tooth enamel in reference to its hardening and softening. J Amer Med Assoc 1912;59:2118–22.
[5] Lynch RJM, Smith SR. Remineralization agents - new and effective or just marketing hype? Adv Dent Res 2012;24:63–7.
[6] Ten Cate JM, Arends J. Remineralization of artificial enamel lesions in vitro. Caries Res 1977;11:277–86.
[7] Kidd EA, Fejerskov O. What constitutes dental caries? Histopathology of carious enamel and dentin related to the action of cariogenic biofilms. J Dent Res 2004;83(Spec No C):C35–8.
[8] Applebaum E. Incipient dental caries. J Dent Res 1932;12:619–27.
[9] Bergman G, Lind PO. A quantitative microradiographic study of incipient enamel caries. J Dent Res 1966;45:1477–84.
[10] Buchalla W, Imfeld T, Attin T, Swain MV, Schmidlin PR. Relationship between nanohardness and mineral content of artificial carious enamel lesions. Caries Res 2008;42:157–63.
[11] Darling AI. The structure of the enamel revealed in dental disease. Arch Oral Biol 1961;4:80–5.
[12] Featherstone JD, Behrman JM, Bell JE. Effect of whole saliva components on enamel demineralization in vitro. Crit Rev Oral Biol Med 1993;4:357–62.
[13] Featherstone JD, ten Cate JM, Shariati M, Arends J. Comparison of artificial caries-like lesions by quantitative microradiography and microhardness profiles. Caries Res 1983;17:385–91.
[14] Magalhães AC, Moron BM, Comar LP, Wiegand A, Buchalla W, Buzalaf MA. Comparison of cross-sectional hardness and transverse microradiography of artificial carious enamel lesions induced by different demineralising solutions and gels. Caries Res 2009;43:474–83.
[15] Orams HJ, Phakey PP, Rachinger WA, Zybert JJ. Ultrastructural changes in the translucent and dark zones of early enamel caries. J Oral Pathol 1980;9:54–61.
[16] Soni NN, Silberkweit M, Parrish BA. A microradiographic-microphotometric and polarized light study of the demineralization pattern in carious lesions. Oral Surg Oral Med Oral 1965;20:321–9.
[17] Delbem ACB, Sassaki KT, Vieira AEM, Rodrigues E, Bergamaschi M, Stock SR, et al. Comparison of methods for evaluating mineral loss: hardness versus synchrotron microcomputed tomography. Caries Res 2009;43:359–65.
[18] Dowker SEP, Elliott JC, Davis GR, Wilson RM, Cloetens P. Three-dimensional study of human dental fissure enamel by synchrotron X-ray microtomography. Eur J Oral Sci 2006;114:353–9.
[19] Huang TTY, He L-H, Darendeliler MA, Swain MV. Correlation of mineral density and elastic modulus of natural enamel white spot lesions using X-ray microtomography and nanoindentation. Acta Biomater 2010;6:4553–9.
[20] Gustafson G. The histopathology of caries of human dental enamel with special reference to the division of the carious lesion into zones. Acta Odontol Scand 1957;15:13–55.
[21] Shellis RP, Hallsworth AS, Kirkham J, Robinson C. Organic material and the optical properties of the dark zone in caries lesions of enamel. Eur J Oral Sci 2002;110:392–5.
[22] Theuns HM, Shellis RP, Groeneveld A, van Dijk JW, Poole DF. Relationships between birefringence and mineral content in artificial caries lesions of enamel. Caries Res 1993;27:9–14.
[23] Kinney JH, Pople JA, Marshall GW, Marshall SJ. Collagen orientation and crystallite size in human dentin: a small angle X-ray scattering study. Calcif Tissue Int 2001;69:27–31.
[24] Kinney JH, Nalla RK, Pople JA, Breunig TM, Ritchie RO. Age-related transparent root dentin: mineral concentration, crystallite size, and mechanical properties. Biomaterials 2005;26:3363–76.
[25] Fratzl P, Paris O, Klaushofer K, Landis WJ. Bone mineralization in an osteogenesis imperfecta mouse model studied by small-angle X-ray scattering. J Clin Invest 1996;97:396–402.
[26] Zizak I, Roschger P, Paris O, Misof BM, Berzlanovich A, Brenstorff S, et al. Characteristics of mineral particles in the human bone/cartilage interface. J Struct Biol 2003;141:208–17.
[27] Kaabar W, Daar E, Bunk O, Farquharson MJ, Laklouk A, Bailey M, et al. Elemental and structural studies at the bone-cartilage interface. Nucl Instrum Methods Phys Res A 2011;652:786–90.
[28] Tanaka T, Yagi N, Ohta T, Matsuo Y, Terada H, Kamasaka K, et al. Evaluation of the distribution and orientation of remineralized enamel crystallites in subsurface lesions by X-ray diffraction. Caries Res 2010;44:253–9.
[29] Tesch W, Eidelman P, Roschger P, Goldenberg F, Klaushofer K, Fratzl P. Graded microstructure and mechanical properties of human crown dentin. Calcif Tissue Int 2001;69:147–57.
[30] Gutierrez P, Piña C, Lara VH, Bosch P. Characterization of enamel with variable caries risk. Arch Oral Biol 2005;50:843.
[31] Märten A, Fratzl P, Paris O, Zaslansky P. On the mineral in collagen of human crown dentine. Biomaterials 2010;31:5479–90.
[32] Jiang H, Liu X-Y, Lim CT, Hsu CY. Ordering of self-assembled nanobiominerals in correlation to mechanical properties of hard tissues. Appl Phys Lett 2005;86:163901.
[33] Gaiser S, Deyhle H, Bunk O, White SN, Müller B. Understanding nano-anatomy of healthy and carious human teeth: a prerequisite for nanodentistry. Biointerphases 2012;7:4.
[34] Fratzl P, Jakob HF, Rinnerthaler S, Roschger P, Klaushofer K. Position-resolved small-angle X-ray scattering of complex biological materials. J Appl Crystallogr 1997;30:765–9.
[35] Yagi N, Ohta T, Matsuo T, Tanaka T, Terada Y, Kamasaka H, et al. Evaluation of enamel crystallites in subsurface lesion by microbeam X-ray diffraction. J Synchrotron Radiat 2009;16:398–404.
[36] Deyhle H, Bunk O, Müller B. Nanostructure of healthy and caries-affected human teeth. Nanomed Nanotechnol 2011;7:694–701.
[37] Beckmann F, Herzen J, Haibel A, Müller B, Schreyer A. High density resolution in synchrotron-radiation-based attenuation-contrast microtomography. Proc SPIE 2008;7078:70781D.
[38] Müller B, Bernhardt R, Weitkamp T, Beckmann F, Bräuer R, Schurigt U, et al. Morphology of bony tissues and implants uncovered by high-resolution tomographic imaging. Int J Mater Res 2007;98:613–21.
[39] Bunk O, Bech M, Jensen TH, Feidenhans'l R, Binderup T, Menzel A, et al. Multimodal x-ray scatter imaging. New J Phys 2009;11:123016.
[40] Kraft P, Bergamaschi A, Broennimann C, Dinapoli R, Eikenberry EF, Henrich B, et al. Performance of single-photon-counting PILATUS detector modules. J Synchrotron Radiat 2009;16:368–75.
[41] Darling AI. The selective attack of caries on the dental enamel. Ann Roy Coll Surg 1961;29:354–69.
[42] Kielbassa AM, Wrbas KT, Schulte Mönting J, Hellwig E. Correlation of transversal microradiography and microhardness on in situ-induced demineralization in irradiated and nonirradiated human dental enamel. Arch Oral Biol 1999;44:243–51.
[43] Soni NN, Brudevold F. Microradiographic and polarized light studies of initial carious lesions. J Dent Res 1959;38:1187–94.
[44] Arends J, Christoffersen J. The nature of early caries lesions in enamel. J Dent Res 1986;65:2–11.
[45] Palamara J, Phakey PP, Rachinger WA, Orams HJ. Laminated zones in carious human dental enamel. J Oral Pathol 1986;15:109–14.
[46] Wefel JS, Harless JD. The use of saturated DCPD in remineralization of artificial caries lesions in vitro. J Dent Res 1987;66:1640–3.
[47] Robinson C, Shore RC, Bonass WA, Brookes SJ, Boteva E, Kirkham J. Identification of human serum albumin in human caries lesions of enamel: the role of putative inhibitors of remineralisation. Caries Res 1998;32:193–9.
[48] Featherstone JD. The continuum of dental caries - evidence for a dynamic disease process. J Dent Res 2004;83(Spec Iss C):C39–42.
[49] Imbeni V, Kruzic JJ, Marshall GW, Marshall SJ, Ritchie RO. The dentin-enamel junction and the fracture of human teeth. Nat Mater 2005;4:229–32.
[50] White SN, Miklus VG, Chang PP, Caputo AA, Fong H, Sarikaya M, et al. Controlled failure mechanisms toughen the dentino-enamel junction zone. J Prosthet Dent 2005;94:330–5.
[51] White SN, Paine ML, Luo W, Sarikaya M, Fong H, Yu Z, et al. The dentino-enamel junction is a broad transitional zone uniting dissimilar bioceramic composites. J Am Ceram Soc 2000;83:238–40.
[52] Almer JD, Stock SR. High energy X-ray scattering quantification of in situ-loading-related strain gradients spanning the dentinoenamel junction (DEJ) in bovine tooth specimens. J Biomech 2010;43:2294–300.
[53] Kidd EA. Clinical threshold for carious tissue removal. Dent Clin N Am 2010;54:541–9.

[54] Al-Jawad M, Streuwer A, Kilconey SH, Shore RC, Cywinski R, Wood DJ. 2D mapping of texture and lattice parameters of dental enamel. Biomaterials 2007;28:2908–14.

[55] Boyde A. A 3-D model of enamel development at the scale of one inch to the micron. Adv Dent Res 1987;1:135–40.

[56] Helmcke J-G. Ultrastructure of enamel. In: Miles AEW, editor. Structural and chemical organization of teeth vol II. New York: Academic Press; 1967. p. 135–6.

[57] Risnes S. Multiplane sectioning and scanning electron microscopy as a method for studying the three-dimensional structure of mature dental enamel. Scanning Microsc 1987;1:1893–902.

[58] White SN, Luo W, Paine ML, Fong H, Sarikaya M, Snead ML. Biological organization of hydroxyapatite crystallites into a fibrous continuum toughens and controls anisotropy in human enamel. J Dent Res 2001;80:321–6.

[59] Zahradnik RT, Moreno EC. Progressive stages of subsurface demineralization of human enamel. Arch Oral Biol 1977;22:585–91.

[60] Eimar H, Ghadimi E, Marelli B, Vali H, Nazhat SN, Amin WM, et al. Regulation of enamel hardness by its crystallographic dimensions. Acta Biomater 2012;8:3400–10.

[61] Frazier PD. Adult human enamel: an electron microscopic study of crystallite size and morphology. J Ultrastruct Res 1968;22:1–11.

Please cite this article in press as: Deyhle H et al. Nanostructure of carious tooth enamel lesion. Acta Biomater (2013), http://dx.doi.org/10.1016/j.actbio.2013.08.024